dynamics studies of strain hardening that at present assume an initial dislocation configuration could incorporate the proposed interatomic-potential-based FEM to solve for the regular stress field solution component, and use the Λ-criterion to nucleate new, embryonic dislocation loops. Likewise, experimental studies of the initiation and early stages of nanoscale deformation via slip, twinning or cracking could be designed to exploit the above-mentioned effects of crystallographic orientation, elastic anisotropy and boundary conditions. □

Received 25 February; accepted 22 May 2002; doi:10.1038/nature00865.

1. Gerberich, W. W., Venkataraman, S. K., Huang, H., Harvey, S. E. & Kohlstedt, D. L. The injection of plasticity by millinewton contacts. *Acta Metal. Mater.* **43,** 1569–1576 (1995).
2. Suresh, S., Nieh, T.-G. & Choi, B. W. Nanoindentation of copper thin films on silicon substrates. *Scripta Mater.* **41,** 951–957 (1999).
3. Kiely, J. D., Jarausch, K. F., Houston, J. E. & Russell, P. E. Initial stages of yield in nanoindentation. *J. Mater. Res.* **15,** 4513–4519 (1999).
4. Gouldstone, A., Koh, H.-J., Zeng, K. Y., Giannakopoulos, A. E. & Suresh, S. Discrete and continuous deformation during nanoindentation of thin films. *Acta Mater.* **48,** 2277–2295 (2000).
5. Kramer, D. E., Yoder, K. B. & Gerberich, W. W. Surface constrained plasticity: Oxide rupture and the yield point process. *Phil. Mag. A* **81,** 2033–2058 (2001).
6. Gouldstone, A., Van Vliet, K. J. & Suresh, S. Nanoindentation: Simulation of defect nucleation in a crystal. *Nature* **411,** 656 (2001).
7. Kelchner, C. L., Plimpton, S. J. & Hamilton, J. C. Dislocation nucleation and defect structure during surface indentation. *Phys. Rev. B* **58,** 11085–11088 (1998).
8. Zimmerman, J. A., Kelchner, C. L., Klein, P. A., Hamilton, J. C. & Foiles, S. M. Surface step effects on nanoindentation. *Phys. Rev. Lett.* **87,** 165507 (2001).
9. Tadmor, E. B., Miller, R. & Phillips, R. Nanoindentation and incipient plasticity. *J. Mater. Res.* **14,** 2233–2250 (1999).
10. Shenoy, V. B., Phillips, R. & Tadmor, E. B. Nucleation of dislocations beneath a plane strain indenter. *J. Mech. Phys. Solids* **48,** 649–673 (2000).
11. Wang, J., Li, J., Yip, S., Phillpot, S. & Wolf, D. Mechanical instabilities of homogeneous crystals. *Phys. Rev. B* **52,** 12627–12635 (1995).
12. Zhou, Z. & Joos, B. Stability criteria for homogeneously stressed materials and the calculation of elastic constants. *Phys. Rev. B* **54,** 3841–3850 (1996).
13. Morris, J. W. & Krenn, C. R. The internal stability of an elastic solid. *Phil. Mag. A* **80,** 2827–2840 (2000).
14. Hill, R. Acceleration waves in solids. *J. Mech. Phys. Solids* **10,** 1–16 (1962).
15. Rice, J. R. in *Theoretical and Applied Mechanics* (ed. Koiter, W. T.) Vol. 1, 207–220 (North-Holland, Amsterdam, 1976).
16. Egami, T., Maeda, K. & Vitek, V. Structural defects in amorphous solids. A computer simulation study. *Phil. Mag. A* **41,** 883–901 (1980).
17. Ray, J. R. Elastic constants and statistical ensembles in molecular dynamics. *Comput. Phys. Rep.* **8,** 109–152 (1988).
18. Ericksen, J. L. in *Phase Transformations and Material Instabilities in Solids* (ed. Gurtin, M. E.) 61–78 (Academic, Orlando, 1984).
19. Tadmor, E. B., Ortiz, M. & Phillips, R. Quasicontinuum analysis of defects in solids. *Phil. Mag. A* **73,** 1529–1563 (1996).
20. *ABAQUS Theory Manual Version 6.1* (Hibbitt, Karlsson and Sorensen, Pawtucket, Rhode Island, 2000).
21. Ackland, G. J., Bacon, D. J., Calder, A. F. & Harry, T. Computer simulation of point defect properties in dilute Fe-Cu alloy using a many-body interatomic potential. *Phil. Mag. A* **75,** 713–732 (1997).
22. Brochard, S., Beauchamp, P. & Grilhe, J. Simulations of dislocation nucleation from atomic size surface steps and grooves. *Mater. Sci. Eng. A* **309–310,** 456–462 (2001).
23. Hwu, C. & Fan, C. W. Solving the punch problems by analogy with the interface crack problems. *Int. J. Solids Struct.* **35,** 3945–3960 (1998).
24. Ercolessi, F. & Adams, J. B. Interatomic potentials from first-principles calculations: the force-matching method. *Europhys. Lett.* **26,** 583–588 (1994).

Supplementary Information accompanies the paper on *Nature*'s website (http://www.nature.com/nature).

Acknowledgements

This work was supported by the Defense University Research Initiative on NanoTechnology (DURINT) on 'Damage- and Failure-Resistant Nanostructured and Interfacial Materials' which is supported at the Massachusetts Institute of Technology by the Office of Naval Research. We thank A. S. Argon for comments. K.J.V.V. acknowledges the National Defense Science and Engineering Graduate Fellowship programme. J.L., T.Z. and S.Y. acknowledge support by Honda R&D, AFOSR, NSF/KDI/DMR, and Lawrence Livermore National Laboratory.

Competing interests statement

The authors declare that they have no competing financial interests.

Correspondence and requests for materials should be addressed to S.Y. (e-mail: syip@mit.edu).

Dynamic fracture by large extraterrestrial impacts as the origin of shatter cones

Amir Sagy*, Ze'ev Reches* & Jay Fineberg†

** Institute of Earth Sciences, † The Racah Institute of Physics, The Hebrew University of Jerusalem, 91904 Jerusalem, Israel*

A large impact by a comet or meteorite releases an enormous amount of energy, which evaporates, melts and fractures the surrounding rocks[1–4]. Distinctive features of such impacts are 'shatter cones', deformed rocks characterized by hierarchical striated features[5,6]. Although such features have been used for decades as unequivocal fingerprints of large-body impacts, the process by which shatter cones form has remained enigmatic. Here we show that the distinctive shatter-cone striations naturally result from nonlinear waves (front waves) that propagate along a fracture front[7–10]. This explains the observed systematic increase of striation angles with the distance from the impact. Shatter-cone networks, typically spanning many scales, can be understood as hierarchical bifurcations of the fracture front, which is generated by the immense energy flux carried by the initial, impact-generated, shock waves. Our quantitative predictions based on this theory are supported by field measurements at the Kentland and Vredefort impact sites. These measurements indicate that shatter cones near to the impact site were formed by fractures propagating at nearly the Rayleigh wave speed of the host rocks, whereas the furthest shatter cones observed (about 40 km from the impact site) were formed by fronts moving more slowly. These results provide insight into impact dynamics as well as dissipative mechanisms in solids subjected to sudden, extremely intense fluxes of energy.

The formidable shock waves generated during large extraterrestrial impacts intensely deform crustal rock[1–4]. Beyond the near-impact region, where rock evaporation and melting prevail, shock-induced structures are dominant[3,11]. Some of the most distinct of these structures are shatter cones (Fig. 1a and b), which are observed in nature only at large impact sites. They range in size from a few centimetres to a few metres[5,11], and generally occur within hierarchic networks—called 'horse-tail' structures[5]—in which cascades of contiguous cones of monotonously decreasing size are observed (Fig. 1b). Although shatter cones are frequently semiconical, complete cones are rare[12,13], and, in many cases, their characteristic striations are observed on nearly planar surfaces[14] (Fig. 1b).

The precise mechanism for shatter-cone formation is unknown. It has been shown that conical shapes could result either from the interaction of shock waves with point inhomogeneities in rocks[15], or from interactions between the main compressive shock and rebound waves[16]. However, these models do not explain the dominant features of shatter cones: characteristic striations (Fig. 1a), the 'horse-tail' cone hierarchy (Fig. 1b), and the rarity of complete cones. Here we present a new model for shatter-cone formation that is based on recent developments in the study of dynamic fracturing[7–10]. This model explains the characteristic features of shatter cones, and its predictions are supported by field observations at the classic impact sites of Vredefort, South Africa, and Kentland, Indiana.

The Kentland impact deformed a thick sequence of Mesozoic carbonate and clastic rocks. A quarry, 1 km^2 in area and 200 m in depth, in the central, uplifted part of this impact provides large, three-dimensional shatter-cone exposures. Our fieldwork reveals that shatter cones are not separable, isolated objects within the rock mass, but are secondary structures that are generated along the

© 2002 Nature Publishing Group

surfaces of large, coherent fractures. At Kentland, for example, the axes of dozens of shatter cones associated with a single large fracture display a well-organized pattern in which the cone axes are directionally aligned over distances of tens of metres. Individual cones range in shape from triangular markings on planar fracture faces to partly conical surfaces that branch away from the host fracture. Examination of the internal cone structure reveals multiple curved, striated surfaces that are essentially secondary branches of the parent fracture (Fig. 2). We have observed up to five levels of hierarchical branches, ranging in size over three to four orders of magnitude. The 'horse-tail' structure of shatter cones may now be understood as a hierarchical network of secondary 'branched' fractures.

These large fractures that generate shatter cones are consistent with tensile fractures formed as a result of the radially propagating shock waves of the impact. Theoretical[17], computational[18–20] and experimental work[21–24] has demonstrated that such impact-generated waves produce large tensile stresses normal to the compressive (radial) direction. These tensile stresses, which are predominantly formed at the waves' trailing edge[18–20,24], will generate tensile fractures that propagate outwards from the axis of impact[19,21–24]. We identify shatter cones with secondary tensile fractures that branch away from the large, primary tensile fractures produced by the impact event. The large-scale coherence induced by the main fracture explains why shatter-cone axes generally point towards the impact centre[5,6]. This picture also explains the hierarchical branched structure of shatter cones (Fig. 2), which is typically observed in high-velocity tensile fracture in both laboratory experiments[25] and in the field[26]. Shatter-cone curvature reflects the initially curved profile observed in these (secondary) branched fractures[25]. The role of shear in shatter-cone formation is secondary. Although a small amount of shear displacement is evident in some shatter cones, no such displacement is observed in most of our samples.

We now turn to the striated surface features that are the hallmark of shatter cones (Figs 1 and 2). Striations are restricted solely to shatter-cone surfaces. Within a given shatter-cone sample, additional (sub-surface) striations may be observed. However, these only occur on well-defined branched fractures that have bifurcated beneath the main fracture (see, for example, Fig. 2a). We now show that shatter-cone striations can also be explained in the framework of dynamic tensile fracture.

Recent work has revealed a type of elastic wave that exists along the one-dimensional front defined by the leading edge of propagating tensile fractures. These waves, termed front waves (FWs), were theoretically predicted to result from the interaction between

Figure 1 The structure of shatter cones. **a**, A typical quasi-conical surface of a shatter cone on a slate sample. Large numbers of striations (elongated traces with a preferred direction) are observed along shatter-cone surfaces. Pairs of striations originate at points along the shatter-cone surface, and emanate outwards at small angles. Striation depths and widths range from ~10 μm to a few millimetres. Scanning electron microscope images reveal that a striation's minimal width corresponds to the grain size of the host rock. **b**, Typical hierarchical, 'horse-tail' structures of a cone-on-cone network on a quasi-planar surface in quartzite. Aligned striations appear on the surface of each cone. Both samples are from the Vredefort impact site.

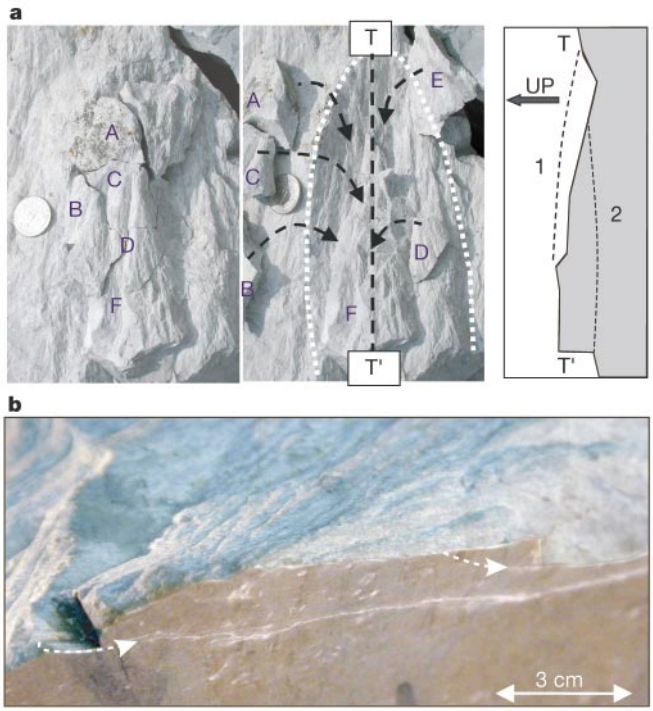

Figure 2 Shatter cones as branched fractures. **a**, Six fragments (labelled A–F) peeled away from the face of a shatter cone reveal a typical branched structure. Left, the fragments in their original positions. Centre, the striated surface of an additional sub-surface cone is clearly visible beneath the removed fragments. This sub-surface cone is formed by a spoon-like branched fracture generated at point T. Right, a crosscut, perpendicular to the surface along the T–T′ line, displays the two branched surfaces. The continuous black line indicates the exposed surfaces after removal of the fragments A–F. The dashed line labelled 1 is the initial (upper) surface (before the removal of A–F). The dashed line labelled 2 indicates an additional unexposed branch. The coin in **a** is 22 mm in diameter. **b**, Although shatter-cone surfaces are highly striated, their sub-surface structure generally consists of relatively few branched fractures. An oblique view of a saw-cut shatter cone displays its sub-surface structure. The bright upper area is its external striated surface. Beneath this surface, two branches are observed. White arrows mark the initial branching locations and consequent propagation directions; the irregular shape of the larger branch indicates additional small-scale branching. Note that the striations are found solely on the fracture surfaces (fractographic features) defined by the branches. Both **a** and **b** are dolomite samples from the Kentland site.

© 2002 Nature Publishing Group

material inhomogeneities and fracture fronts[7–9]. Experiments[10] have shown that FWs, initiated by localized inhomogeneities, create characteristic tracks on the fracture surface (Fig. 3). Pairs of tracks emanate from a local inhomogeneity with a relative angle, α, described by the relation $\cos(\alpha/2) = V/V_{FW}$, where V and V_{FW} are, respectively, the propagation velocities of the fracture front and the FW (Fig. 3). V_{FW} is approximately $(0.96–1.0)V_R$ (refs 7–9), where V_R, the Rayleigh wave speed of the material, is the maximum speed at which a tensile crack can propagate[27]. This maximal fracture velocity is independent of both the intensity of the tensile stress driving the fracture and the velocity of the shock wave responsible for the loading. Angles greater than $\alpha = 105°$ ($V < 0.6V_R$; ref. 25) have been observed in laboratory experiments (Fig. 3). Because the stress needed to drive a crack increases precipitously beyond this velocity, smaller angles, corresponding to higher fracture velocities, are nearly impossible to achieve under laboratory conditions.

We now postulate that each striation on a shatter-cone surface is a FW track formed along the rapidly propagating fracture front generated by the impact. This would predict that: (1) the angles between striations at a given shatter-cone site should fall within a narrow range, because α is solely determined by V/V_{FW}; and (2) α should systematically increase with the distance from the impact centre, as the fracture velocity will decrease with the decreasing stress away from the centre.

The Vredefort impact in South Africa (Fig. 4a) provides an excellent test of this hypothesis. The Vredefort site, created about two billion years ago, is one of the largest impact structures on Earth, about 200 km in diameter, and countless shatter cones are exposed within a belt around its centre[4,14,28]. We analysed shatter cones at 22 sites distributed in the northern section of the Vredefort structure, at distances ranging from 14 km to 37.5 km from its centre (Fig. 4a). The sites are located on exposures of granites, quartzite, slates, chert and andesites, and cover most of the range of shatter-cone distribution in the Vredefort site. Semiconic and semiplanar striated surfaces are well-developed in the fine-grain rocks (slates and quartzite), and are less developed in the coarse-

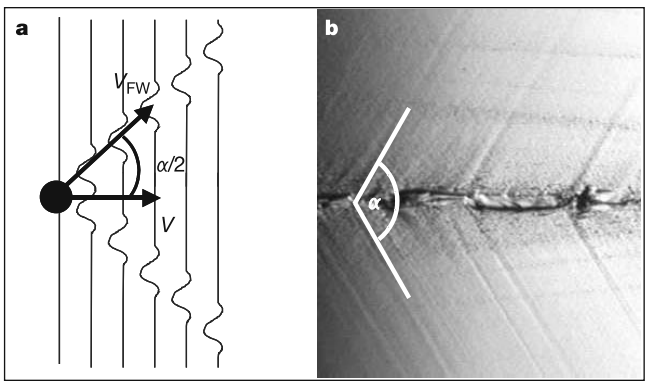

Figure 3 Fracture front waves, FWs, are generated by the interaction of a dynamic fracture front with a localized inhomogeneity. **a**, A schematic presentation of FWs generated by an inhomogeneity (filled circle). Shown are sequential locations of the leading edge of a fracture (a 'fracture front') propagating from left to right with velocity V. Each line marks the position of the fracture front at successive, evenly spaced, time intervals. Two counter-propagating FWs, emitted at the inhomogeneity, propagate along the front with velocity V_{FW} with respect to their initiation point. FWs create structure within the fracture plane that can be observed as characteristic tracks on the fracture surface. The propagation velocity, V, can be determined from the angle α by[10]: $\cos(\alpha/2) = V/V_{FW}$. **b**, Photograph of a fracture surface in glass, with FW tracks generated by localized inhomogeneities induced by the spontaneous formation of small branched fractures[25] ('micro-branches'). As indicated by $\alpha \approx 105°$, this fracture propagated from left to right at $V \approx 0.65V_{FW}$.

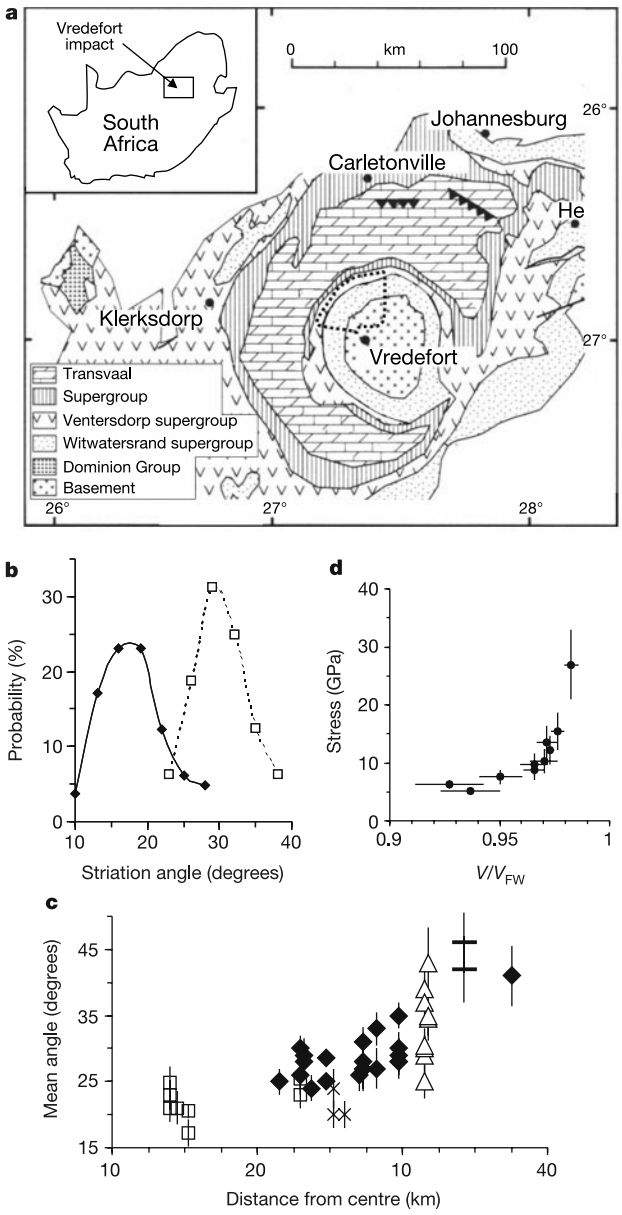

Figure 4 Shatter-cone measurements at the Vredefort impact site. **a**, A simplified map of the Vredefort impact structure[30]. The locations of the 22 sites at which shatter cones were studied are denoted by the dotted lines. Their present location is a cumulative result of three deformation stages: intra-impact excavation, post-impact relaxation and regional erosion over the last 2 billion years[4]. **b**, In a given shatter cone, the angles between striations are narrowly distributed. Histograms of striation angles, α, measured in slate (diamond symbols) and quartzite (squares) samples, found at different sites are presented. **c**, The mean striation angles, α, systematically increase with the distance from the impact site. Shown are mean striation angles corresponding to granite (squares), quartzite (filled diamonds), slates (crosses), andesite (triangles), and chert (bars). Error bars are 1 s.d. of the measured angles at each site. We ascribe the scatter of α at a given site to variance of the mechanical properties of the rocks. **d**, The relation between the fracture propagation velocity, calculated by $\cos(\alpha/2) = V/V_{FW}$, and the local value of the calculated compressive stresses[4] induced by the Vredefort impact event. Note the sharp, highly nonlinear, increase of the stress needed to drive propagation velocities that approach the maximal limit of $V_R \approx V_{FW}$. Tensile stresses in the wake of the compressive shock actually drive the fractures. These, which have not been explicitly calculated for the Vredefort event, are of the same order of magnitude as compressive components[17–19]. Our evaluation of the impact stresses at the measurement sites is based on the numerical modelling of the first two deformation stages for the Vredefort crater by Turtle and Pierazzo[4]. Their best model was calculated for a 10-km-diameter impactor having an impact velocity of 20 km s^{-1}. We assume 5–10 km of erosion[4,30].

© 2002 Nature Publishing Group

grained rocks (granite). We used samples from the 22 sites to measure the angle α between pairs of striations. At every site, well-defined striation angles were measured on a number of samples. As predicted, the angles measured within an individual sample are relatively constant with a typical standard deviation of 5° (Fig. 4b). In addition, the mean striation angles systematically increase from 17° to 46° with the distance from the impact centre (Fig.4c). Thus, both the narrow angular distributions and the systematic increase of mean angles are consistent with our postulate that the striations are formed by front waves.

Using $\cos(\alpha/2) = V/V_{FW} \approx V/V_R$, we calculated the fracture velocities from the measured angles (Fig. 4c). The specific values of V_R in the samples are immaterial, because the angle α measures only the normalized fracture velocity, V/V_{FW}. We find that V approaches $0.98V_R$ at approximately 15 km from the impact centre, and decreases to $\sim 0.9V_R$ at 35–40 km from the centre. Thus, shatter cones are observed within the narrow range of fracture velocities above $0.9V_R$. Using the calculated spatial distribution of the stress applied by the shock wave at Vredefort[4], Fig. 4d indicates a precipitous rise of the applied stresses with fracture velocity. This increase is consistent with laboratory experiments[29] at lower velocities, and amply demonstrates why mean fracture velocities approaching V_R are never observed in the laboratory. At the larger striation angles, we find that shatter cones are not as easily recognized, as clear striations are less frequently observed, possibly because their amplitudes are reduced at lower energy flux levels.

We have shown that shatter cones are branched tensile fractures. Shatter-cone striations are the preserved tracks of fracture front waves. Analysis of the striations shows that shatter cones develop only at extreme propagation velocities, between $0.9V_R$ and the maximal permitted velocity of V_R. The angles of the striations (α), which are shown to increase systematically with the distance from the impact, reflect both the stresses and the energy flux driving the fracture at a given site, and may be used as a general tool to evaluate extreme local stresses in the field. Our results also demonstrate that such rapid fracture propagation in intact solids necessitates extremely high-energy fluxes, supplied naturally only by large impactors. □

Received 5 February; accepted 10 June 2002; doi:10.1038/nature00903.

1. Melosh, H. J. Impact ejection, spallation, and the origin of meteorites. *Icarus* **59,** 234–260 (1984).
2. Melosh, H. J. *Impact Cratering: A Geologic Process* (Oxford Univ. Press, New York, 1989).
3. French, B. M. *Traces of Catastrophe. Handbook of Shock-metamorphic Effects in Terrestrial Meteorite Impact Structures* (Lunar and Planetary Institute, Houston, 1998).
4. Turtle, E. P. & Pierazzo, E. Constraints on the size of the Vredefort impact crater from numerical modeling. *Meteorit. Planet. Sci.* **33,** 483–490 (1998).
5. Dietz, R. S. in *Shock Metamorphism of Natural Materials* (eds French, B. M. & Short, N. M.) 267–285 (Mono Book Corp., Baltimore, 1969).
6. Sharpton, V. L., Dressler, B. O., Herrick, R. R., Schnieders, B. & Scott, J. New constraints on the Slate Islands impact structure, Ontario, Canada. *Geology* **24,** 851–854 (1996).
7. Morrissey, J. W. & Rice, J. R. Crack front waves. *J. Mech. Phys. Solids* **46,** 467–487 (1998).
8. Morrissey, J. W. & Rice, J. R. Perturbative simulations of crack front waves. *J. Mech. Phys. Solids* **48,** 1229–1251 (2000).
9. Ramanathan, S. & Fisher, D. S. Dynamics and instabilities of planar tensile cracks in heterogeneous media. *Phys. Rev. Lett.* **79,** 877–880 (1997).
10. Sharon, E., Cohen, G. & Fineberg, J. Propagating solitary waves along a rapidly moving crack front. *Nature* **410,** 68–71 (2001).
11. Milton, D. J. in *Impact and Explosion Cratering; Planetary and Terrestrial Implications* (eds Roddy, D. J., Pepin, R. O. & Merrill, R. B.) 703–714 (Pergamon, New York, 1977).
12. Roy, D. W. Shatter cone geometry and description procedure. *Tectonophysics* **60,** T37–T42 (1979).
13. Albat, H. M. & Mayer, J. J. Megascopic planar shock fractures in the Vredefort Structure; a potential time marker? *Tectonophysics* **162,** 265–276 (1989).
14. Nicolaysen, L. O. & Reimold, W. U. Vredefort shatter cones revisited. *J. Geophys. Res. B* **104,** 4911–4930 (1999).
15. Johnson, G. P. & Talbot, R. J. *A Theoretical Study of the Shock Wave Origin of Shatter Cones* Thesis (Air Force Inst. Technol., Wright-Patterson Air Force Base).
16. Gash, P. J. S. Dynamic mechanism for the formation of shatter cones. *Nature* **230,** 32–35 (1971).
17. Shibuya, T. & Nakahara, I. The semi-infinite body subjected to a concentrated impact load on the surface. *Bull. Jpn Soc. Mech. Eng.* **11,** 983–992 (1968).
18. Asphaug, E. *et al.* Mechanical and geological effects of impact cratering on Ida. *Icarus* **120,** 158–184 (1996).
19. Camacho, G. T. & Ortiz, M. Computational modelling of impact damage in brittle materials. *Int. J. Solids Struct.* **33,** 2899–2938 (1996).
20. Melosh, H. J., Ryan, E. V. & Asphaug, E. Dynamic fragmentation in impacts — Hydrocode simulation of laboratory impacts. *J. Geophys. Res. E* **97,** 14735–14759 (1992).
21. Field, J. E. Brittle fracture: its study and application. *Contemp. Phys.* **12,** 1–31 (1971).
22. Ahrens, T. J. & Rubin, A. M. Impact-induced tensional failure in rock. *J. Geophys. Res. E* **98,** 1185–1203 (1993).
23. Polanskey, C. A. & Ahrens, T. J. Impact spallation experiments; fracture patterns and spall velocities. *Icarus* **87,** 140–155 (1990).
24. Arakawa, M., Shirai, K. & Kato, M. Shock wave and fracture propagation in water ice by high velocity impact. *Geophys. Res. Lett.* **27,** 305–308 (2000).
25. Sharon, E. & Fineberg, J. Microbranching instability and the dynamic fracture of brittle materials. *Phys. Rev. B* **54,** 7128–7139 (1996).
26. Sagy, A., Reches, Z. & Roman, I. Dynamic fracturing; field and experimental observations. *J. Struct. Geol.* **23,** 1223–1239 (2001).
27. Freund, L. B. *Dynamic Fracture Mechanics* (Cambridge Univ. Press, Cambridge, 1990).
28. Henkel, H. & Reimold, W. U. Integrated geophysical modelling of a giant, complex impact structure; anatomy of the Vredefort Structure, South Africa. *Tectonophysics* **287,** 1–20 (1998).
29. Dally, J. W. Dynamic photoelastic studies of fracture. *Exp. Mech.* **19,** 349–361 (1979).
30. Therriault, A. M., Grieve, R. A. F. & Reimold, W. U. Original size of the Vredefort Structure; implications for the geological evolution of the Witwatersrand Basin. *Meteorit. Planet. Sci.* **32,** 71–77 (1997).

Acknowledgements

We thank W. U. Reimold and E. G. Charlesworth for information and hospitality at the Vredefort site; the Rogers Group's Newton County quarry for their hospitality at the Kentland site; and G. Cohen for assistance. This work was supported by the United States–Israel Binational Fund.

Competing interests statement

The authors declare that they have no competing financial interests.

Correspondence and requests for materials should be addressed to J.F. (e-mail: jay@vms.huji.ac.il).

Climate-mediated energetic constraints on the distribution of hibernating mammals

Murray M. Humphries*†, Donald W. Thomas‡ & John R. Speakman*§

* *Department of Zoology, University of Aberdeen, Aberdeen AB24 3TZ, UK*
† *Department of Biological Sciences, University of Alberta, Edmonton, Alberta T6G 2E9, Canada*
‡ *Département de Biologie, Université de Sherbrooke, Sherbrooke, Québec J1K 2R1, Canada*
§ *Rowett Research Institute, Bucksburn, Aberdeen AB21 9BS, UK*

To predict the consequences of human-induced global climate change, we need to understand how climate is linked to biogeography[1]. Energetic constraints are commonly invoked to explain animal distributions, and physiological parameters are known to vary along distributional gradients[2]. But the causal nature of the links between climate and animal biogeography remain largely obscure[2,3]. Here we develop a bioenergetic model that predicts the feasibility of mammalian hibernation under different climatic conditions. As an example, we use the well-quantified hibernation energetics of the little brown bat (*Myotis lucifugus*) to parameterize the model[4]. Our model predicts pronounced effects of ambient temperature on total winter energy requirements, and a relatively narrow combination of hibernaculum temperatures and winter lengths permitting successful hibernation. Microhabitat and northern distribution limits of *M. lucifugus* are consistent with model predictions, suggesting that the thermal dependence of hibernation energetics constrains the biogeography of this species. Integrating projections of climate change into our model predicts a pronounced northward range expansion of hibernating bats within the next 80 years. Bioener-

© 2002 Nature Publishing Group